Soft Matter

Tuning assembly structures of hard shapes in confinement via interface curvature

Journal:	*Soft Matter*
Manuscript ID	SM-ART-04-2022-000545.R1
Article Type:	Paper
Date Submitted by the Author:	30-Jun-2022
Complete List of Authors:	Skye, Rachael; Cornell University, Materials Science and Engineering Teich, Erin; University of Pennsylvania, Bioengineering Dshemuchadse, Julia; Cornell University, Department of Materials Science and Engineering

Soft Matter

ARTICLE TYPE

Cite this: DOI: 00.0000/xxxxxxxxxx

Tuning assembly structures of hard shapes in confinement *via* interface curvature

Rachael S. Skye,[a] Erin G. Teich,[b] and Julia Dshemuchadse*[a]

Received Date
Accepted Date

DOI: 00.0000/xxxxxxxxxx

Assembly in confinement is a problem of great interest in colloidal structure design, plasmonics, photonics, and industrial packaging. Along with the range of design choices provided by particle shape and attraction or repulsion, confined systems add an additional layer of complexity through the interactions between particles and the container holding them. The range of possible behaviors produced by these systems remains largely unexplored, yet has profound consequences on the resultant assembled structure. Here, we address this problem by exploring how the assembly of hard tetrahedral particles is affected by a spherical container. We simulate particle assemblies in containers holding 4 to $10,000$ particles and analyze the range of resultant structures. We find that the presence of a curved wall causes organization into distinct concentric shells in containers holding up to thousands of particles. In addition, we see that wall curvature affects structural motifs in systems as large as $10,000$ particles, promoting local environments that maximally conform to the wall and providing a seed for the propagation of these motifs into the interior of the container. Through this work, we show how confining interfaces can be used to promote the assembly of structures markedly distinct from those seen in the more commonly studied bulk systems.

1 Introduction

The dense packing of shapes is an age-old optimization problem.[1–4] Given a particular shape—sphere, cube, *etc.*—into what structure can it be expected to pack? In recent years, advances in computational techniques have allowed researchers to explore the dense packings of a myriad of shapes.[5–7] In addition, experimental techniques have realized a diverse array of shapes in particle synthesis, including tetrahedral silica–polystyrene core-shell particles,[8] supramolecular tetrahedral assemblies,[9] and faceted metal[10] or semiconductor nanoparticles.[11]

The majority of these studies assume a bulk crystal of near-infinite size. However, a less-explored question is: what happens if the crystal is not infinite? Previous studies have focused on the assembly of spheres in spherical containers[12–15] or other geometries,[16–18] and only more recently has the focus extended to polyhedra.[19–21] Researchers have developed techniques to experimentally realize spherical assemblies of colloidal particles on the mesoscale, for example through evaporating emulsion droplets in a suspension.[14,21–25] Such assemblies allow control over the number of particles in the container. Several studies have also explored other geometries, including polyhedra confined between flat walls,[26–28] within cylinders,[29] or on the surface of cylinders and curved interfaces.[30]

Thus far, only a limited sampling of anisotropic particles has been investigated, such that we still lack a complete understanding of how the diverse particle shapes that we can synthesize will interact with a confining wall. Here, we address this gap through studying a family of hard particle shapes in spherical confinement *via* Monte Carlo simulations. By focusing our efforts on a single family, we study how continuous gradations in particle geometry affect assembly behavior, allowing us to work towards an understanding of particle assembly that does not rely on individually simulating every possible geometry. We have chosen to focus on an experimentally relevant class of shapes, vertex-truncated tetrahedra,[9,11,31] which exhibit a wide array of behaviors. The hard Platonic tetrahedron assembles a dodecagonal quasicrystal[32]—the first observation of a quasicrystal formed only from hard interactions. Truncated tetrahedra assemble several structure types, among them diamond,[33] a structure of great interest on the mesoscale because of its potential to exhibit a full, three-dimensional photonic band gap in the visible-light regime.[34] Through studying the behavior of this shape family, we contribute towards an understanding of how the geometry of particles interacts with the geometry of the container in which those particles are assembled.

2 Methods

Simulations were performed using the Hard-Particle Monte Carlo (HPMC) algorithm implemented in the HOOMD-blue software

[a] *Department of Materials Science and Engineering, Cornell University; E-mail: jd732@cornell.edu*
[b] *Department of Bioengineering, University of Pennsylvania*

package.[35–38] Data management was supported by the signac data management framework,[39–41] analysis of the final structures was performed using the freud package,[42,43] and visualizations were created using OVITO[44,45] and Plato.[46]

This study focuses on hard particles; that is, particles which only interact *via* volume exclusion. Hard particles crystallize with increasing pressure and their interactions are dominated by entropic effects.[5,47–49] To explore the effects of confinement and wall curvature on particle assembly and interparticle motifs, we use a continually shrinking, hard-walled spherical container. Following the protocol established by Teich *et al.*,[19] particles were initialized on a random grid at low pressures and compressed in an *NPT* ensemble, and the final quenched structures were analyzed. The pressure was increased from $\beta P = 0.1$ to $\beta P = 100$ over 10^7 Monte Carlo (MC) steps, where $\beta = 1/k_B T$. In trial runs, it was confirmed that changes in packing fraction are minimal for all shapes at pressures well below this final value. One MC *step* in HOOMD-blue is defined as 4 attempts to move each particle. In order to explore the effects of container size and curvature at equal pressure, the number of particles in the container is increased for consecutive simulations. This simulation protocol uses small Monte Carlo step sizes to approximate the kinetics of hard particle systems under increasing pressure.[50] Assembly occurs en route to a final, high pressure value, allowing us to study the resultant structure. This quenched structure is usually distinct from the densest packed structure, in particular for large systems.

Additionally, simulations with periodic boundary conditions were performed to compare confined systems to the bulk. A slightly different compression procedure is necessary to induce crystallization in these conditions (and to allow for efficiently sampling larger system sizes). Bulk simulations contained 4096 particles. In addition to volume changes, we also allowed for separate Monte Carlo moves in simulation box tilt and aspect ratio. The system was compressed to the crystallization packing fraction,[33] held for 10^6 steps, and then compressed over a further 10^6 steps to $\beta P = 100$. Two types of these simulations were performed; one which had periodic boundary conditions in three dimensions, and one with a wall simulating a zero-curvature container, with periodic boundaries in two dimensions and a hard wall in the third. In all simulations, allowable Monte Carlo moves were particle translations, particle rotations, and box or wall radius changes, all of which were tuned to an acceptance rate of 0.2.[51]

In order to explore particle shape space continuously, we simulated hard tetrahedra with a range of vertex truncations. We constructed each truncated tetrahedron as the volume bounded by the intersection of a precise set of four planes with a Platonic tetrahedron. These planes are normal to the vectors pointing to each tetrahedron vertex, and are located at distance c from the origin.[6] We then resized the resultant shape to unit volume according to a previously outlined normalization procedure.[37] In this way, a tetrahedron can be transitioned smoothly to an octahedron by continually truncating the vertices. The transformations are characterized by the shape parameter c, which falls in the range $c \in [1,3]$, with $c = 3$ representing the tetrahedron and $c = 1$ the octahedron.[6]

We sampled this range of c values with ten evenly spaced points. In addition, three specific shapes were given particular attention: $c = 3$, $c = 2$, and $c = 5/3$, corresponding to the Platonic tetrahedron (PT), the space-filling truncated tetrahedron (STT; which tiles space[33]), and the Archimedean truncated tetrahedron (ATT; which has edges all equal in length), respectively. These truncations also mark different points in the known bulk-phase behavior: tetrahedra assemble into a dodecagonal quasicrystal, ATTs into a diamond-type structure, and STTs lie in a region that tends to form amorphous solids.[33] Due to its differing symmetry (point group $m\bar{3}m$ instead of $\bar{4}3m$) and bulk assembly behavior, the Platonic octahedron at $c = 1$ was excluded from in-depth analysis in this study.

3 Results

In our simulations, we observe that the primary feature of spherically-confined systems is their organization into a series of concentric shells. Representative samples of the structures formed by tetrahedra with low and high levels of truncation are compared in Fig. 1a. At small N, in high-curvature containers, systems tend towards distinct structures with few variations. As N increases, the final structure conforms to the spherical wall and begins to form a spherical shell with a void in the center, where the vertices cluster. Additional particles are added in the outer shell, expanding it until the void is large enough to accommodate a particle in the center.

The development of a core–shell structure can be detected using the fraction of the container that is filled by particles—the spherical packing fraction ϕ_{sphere}. As observed in a previous study,[19] ϕ_{sphere} is closely linked to the exact structure of small clusters, and changes in ϕ_{sphere} show the variability across replicated Monte Carlo simulations. Here we concentrate on the large, discontinuous change in packing fraction caused by the development of a second shell within the system, which is illustrated in Fig. 1b. The branch at higher packing fraction corresponds to the evolution of the single-shell state, and the emerging lower branch corresponds to the two-shell state. The fraction of replicas in each branch indicates the accessibility of that state. At large-enough values of N, the single-shell state becomes unfavorable and the probability of observing it becomes vanishingly small. Fig. 1c maps the probability of forming a one- *vs.* a two-shell structure across shape space. A shape that always forms one-shell structures is indicated by dark purple, and those that only form the two-shell structure by yellow. For each shape, we observe a transition range over a few N in which both structures are possible. The N-values of this transition decrease with increasing vertex truncation. For the Platonic tetrahedron, the vertices cluster to fill the center of the container. As these vertices are truncated, a void in the center of the container is created and grows. The two-shell structure forms when this void is large enough that it is favorable to place a particle in it.

Studying packing fraction is most useful for small numbers of particles N, where minute differences in structure can have a large effect on packing fraction. As N increases, different particle arrangements cannot be distinguished *via* packing fraction ϕ_{sphere}, and other methods of structural analysis must be em-

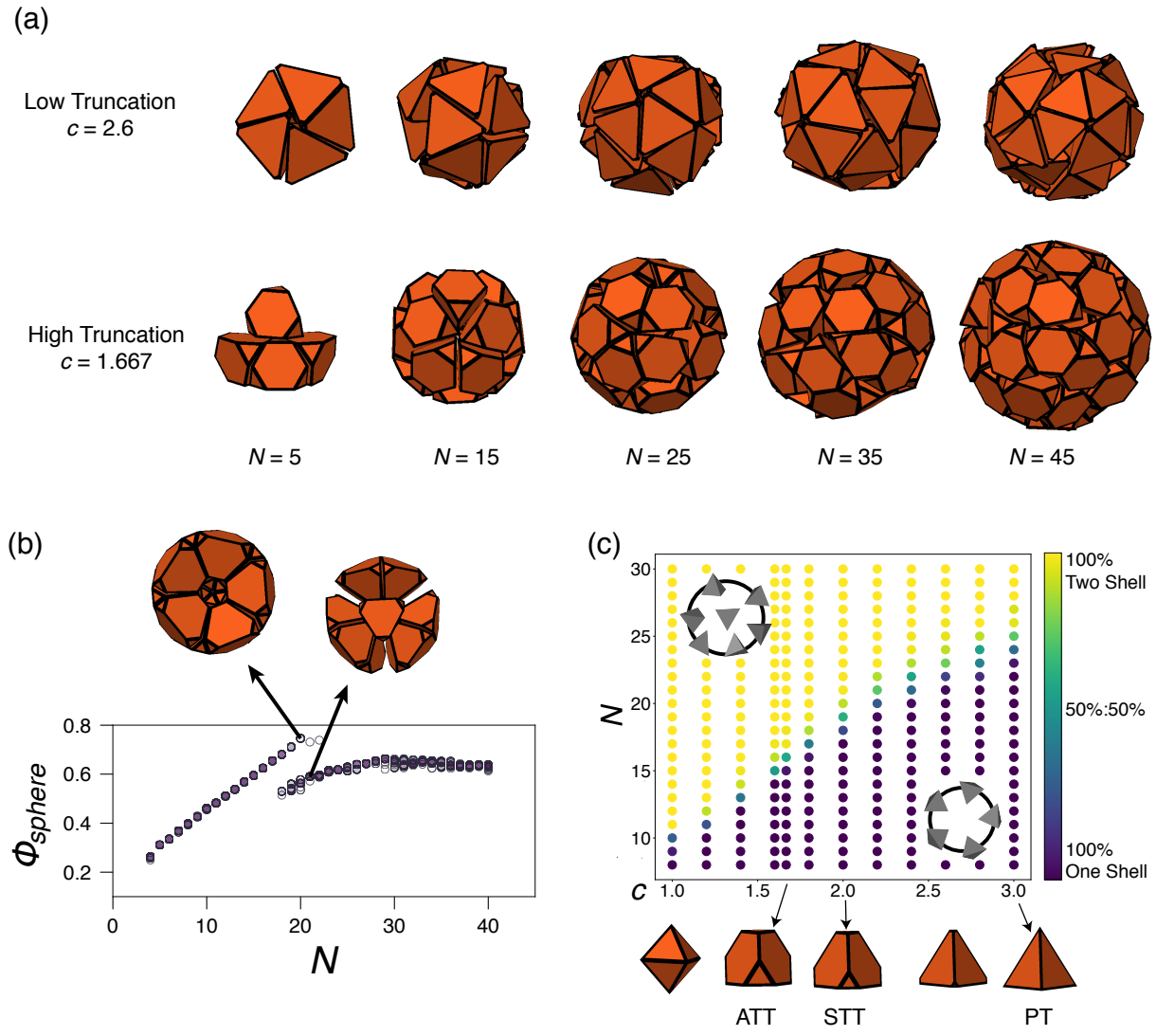

Fig. 1 Small-N systems of spherically confined truncated tetrahedra. **(a)** Comparison of example replicas for a range of system sizes, at low truncation ($c = 2.6$) and high truncation ($c = 1.667$). **(b)** Packing fractions of 50 replicas at small system sizes $N = 4$ to 40, for $c = 2.0$. Each replica is represented by a partially translucent marker, such that stronger color saturation indicates that a structure is more common. The discontinuity around $N = 20$ indicates the split between one- and two-shell structures. **(c)** Occurrence of one- *vs.* two-shell structures across truncations. Purple indicates a system where all 50 replicas exhibit one-shell structures, and yellow indicates systems that always exhibit two-shell structures. As the tetrahedra become more truncated (decreasing c), the system size N at which the transition occurs decreases.

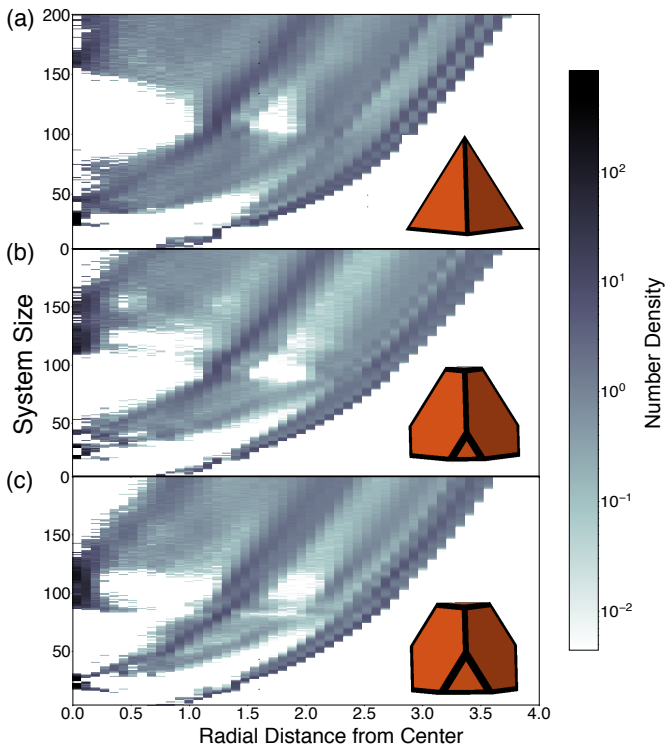

Fig. 2 Container-centered radial distribution functions for hard polyhedra in spherical confinement (with $N = 4$ to 200 particles per simulation): **(a)** Platonic tetrahedra (PT), **(b)** space-filling truncated tetrahedra (STT), and **(c)** Archimedean truncated tetrahedra (ATT). Color intensity corresponds to the number density of particles on a logarithmic scale, discretized to spherical shells of width 0.08. High-density bands conforming to the surface of the container dominate the outer shells, and inner shells grow with them. In each shape, the development of 3 separate shells can be seen.

ployed. To study the development of layered structures, we use a variation of the radial distribution function (RDF) that is adapted to the confined geometries investigated: in this modified RDF, the center of the spherical container is defined as $r = 0$, and a histogram is calculated which shows the number density of particles within a spherical shell a distance r from the origin. We average these histograms over all replicas, which allows us to study the overall changes in the system with N (and, by proxy, container radius). In Fig. 2, we show the development of this container-centered RDF across system sizes $N = 4$ to 200 for three key shapes: Platonic tetrahedra (PT), space-filling truncated tetrahedra (STT), and Archimedean truncated tetrahedra (ATT). The development of pronounced shell structures with increasing N is clear: initially, a second shell develops around $N = 20$ for each shape. The two shells then grow outward as N increases, with high-density shells separated by low-density regions. The development of a third shell can also be identified, at around $N = 87$ for ATTs, $N = 112$ for STTs, and $N = 155$ for PTs.

The radial distribution function describes global structural changes as the container grows. To investigate the behavior of individual particles in their local environments, different tools are needed. In systems of anisotropic particles, local motifs can be quantified *via* particle–particle misorientation angles—the minimum angle that a particle must be rotated in order to match the orientation of a second, reference particle.[52] Different crystal structures exhibit characteristic distributions of misorientation angles; thus, these distributions can be used to quantify the assembled structures by their local motifs. Systems of tetrahedral particles can be characterized by two predominant motifs: misorientation angles of 90° and approximately 70.5°.[53] As is shown in Fig. 3a, both of these angles correspond to particles that are aligned facet-to-facet. A 90° misorientation features the vertices of one particle aligned with the edge midpoints of the other, while a *ca.* 70.5° misorientation corresponds to the vertices of both particles in alignment with one another. The "anti-aligned" 90° misorientation angle is characteristic of the diamond-type structure formed by highly truncated tetrahedra (*e.g.*, ATT), whereas Platonic tetrahedra favor the vertex-to-vertex "aligned" motif, which is characteristic of the dodecagonal quasicrystal that they assemble.

The development of local motifs in spherically-confined assemblies with increasing numbers of particles N is mapped in Fig. 3 *via* three sets of stacked histograms for the three shapes: PTs, STTs, and ATTs. Here, for each particle we consider the set of all misorientations with respect to its nearest neighbors, as determined by a cutoff radius from the particle-to-particle radial distribution function. At small N in high-curvature containers, all truncations favor the aligned motif: the vertices cluster in the center of the spherical container, maximizing packing density. Tetrahedra, which also favor this motif in the bulk, only show intermittent deviations from this dominant motif as the second shell is developed around $N = 23$. As N increases, the decreasing curvature of the container allows tetrahedral particles to assemble into their locally preferred aligned motif.

STTs exhibit a broader distribution of angles, consistent with their position in the disordered region of the self-assembly phase diagram:[54] the bulk phase is characterized by a competition between aligned and anti-aligned local motifs.[53] Although the aligned motif is always dominant in confinement, there is an increase in prevalence of the anti-aligned motif at high numbers of particles, *i.e.*, in large containers; this motif is less prevalent in the quenched bulk structure, where the aligned motif dominates. Even in system sizes of $N = 10,000$, the container walls influence the structural behavior of this shape throughout essentially the entire system (see Fig. 4).

In contrast, spherically confined assemblies of ATTs show a monotonic transition, from aligned motif dominance in small containers to anti-aligned dominance in large containers. As for the STT, the transition is gradual (see Fig. 3), with the prevalence of the anti-aligned motif increasing and the occurrence of the aligned motif decreasing as the number of particles—and therefore the container size—grows. The evolution from confined to bulk behavior is a continuous change in the frequency of local particle environments, rather than an abrupt transition of the entire system, and the transition is not complete at system sizes of $N = 10,000$. Each shape displays a signature noticeably distinct from the bulk. We propose that heterogeneous nucleation is part of the cause: the presence of walls appears to lower the energy

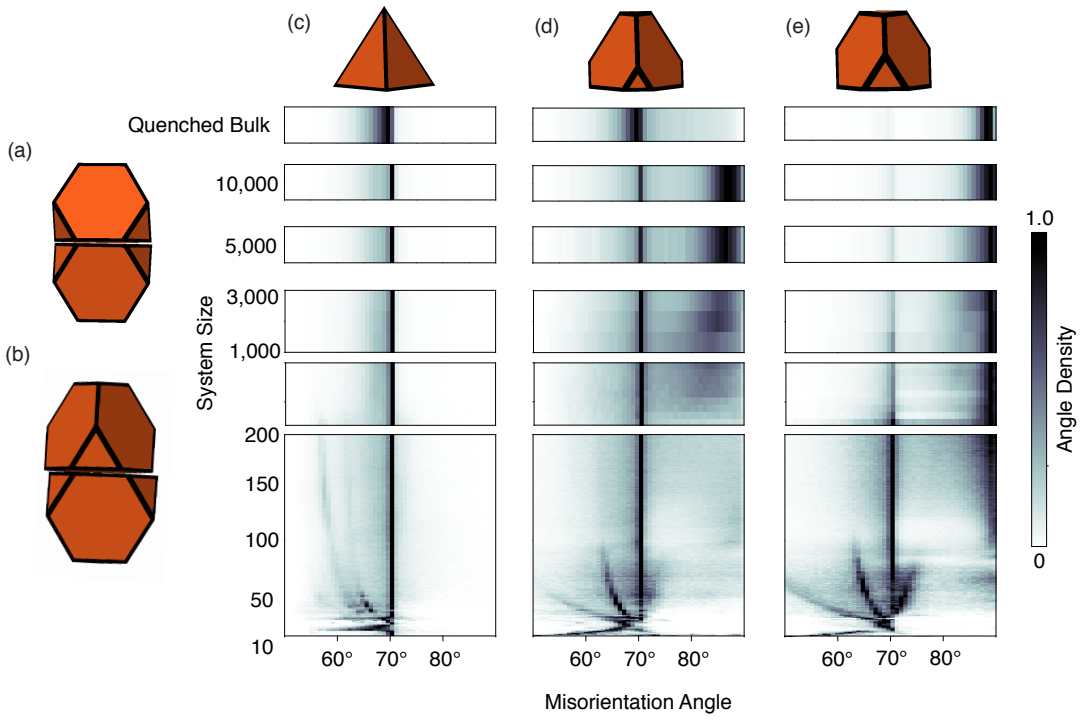

Fig. 3 Distribution of misorientation angles for systems in spherical confinement ($N = 10$ to $10,000$) *vs.* in the bulk. The key misorientations for assemblies of tetrahedra are **(a)** the aligned motif at $\approx 70.5°$, and **(b)** the anti-aligned motif at $90°$. Darker colors represent an increased frequency of specific misorientations at each N, normalized so that the maximum for each system size is 1. For small numbers N, particles of all three shapes favored the aligned motif at $70.5°$ with the overall behavior varying strongly with N. **(c)** For PTs, this motif persists up to large containers. **(d)** For STTs, the prevalence of the anti-aligned motif near $90°$ increases with system size, but vanishes in the bulk. **(e)** For ATTs, the frequency of the anti-aligned motif increases monotonically with N.

barrier to assembly. This effect causes the growth of larger and more ordered crystal grains in systems of ATTs, explaining a narrowing of the misorientation angle peak. However, STTs exhibit a distinctly *different* motif in the confined case, which is not observed in the bulk, and whose nucleation seems to be catalyzed by the container walls.

When observing the split between motifs in the ATTs and STTs, a natural question occurs: are these motifs segregated into different regions of the assembly, or are they evenly distributed across the container? By visual inspection of a representative sample of a large system, we can examine the partitioning of motifs. Platonic tetrahedra exhibit uniformly distributed aligned motifs, and by $N = 10,000$ (Fig. 4a,d) the concentric-shell structure is no longer apparent and the motif distribution is similar to the bulk, with the wall only influencing the outermost layer of particles.

For STTs and ATTs, a very different pattern emerges: the anti-aligned motif dominates in distinct layers near the wall, while the predominance of other motifs grows near the core, and the concentric shells lose coherency. Each surface layer corresponds approximately to a section of the $\{111\}$-oriented layer of the diamond-type structure assembled by ATTs in the bulk, but with the motifs curved slightly to accommodate the wall. The layers are incommensurate with each other, due to the decreasing curvature towards the center of the container, preventing the development of a robust diamond-type structure throughout. Near the center, each shape adopts its bulk structure, with ATTs forming small grains of diamond-type structure that grow into larger wedge-shaped grains. This assembly is approximately icosahedrally twinned, as has been reported previously in assemblies of confined spheres.[24] This similarity is due to the fact that the diamond crystal structure preferred by ATTs corresponds to ABC stackings of dense-packed layers (two-dimensional dense packings of spheres on a triangular tiling *vs.* layers of alternately oriented ATTs, each on a triangular tiling), equivalent to the local environments of particles arranged in a Laves phase-type structure.[55] These layers can form twinned stacking faults (*e.g.*, ABA instead of ABC) without disrupting the dense packing. STTs appear to form a similar structure near the surface for *ca.* three layers, but near the center of the container the diamond-like layering is disrupted and the aligned motif dominates instead.

From these observations, we can hypothesize that the presence of a wall that is nearly flat—compared with the particle size—promotes the anti-aligned motif. To investigate this, we simulated the theoretical zero-curvature case: if the container were to be expanded to infinite size, the walls would become completely flat. We therefore performed simulations in a cubic box with parallel flat walls on two opposite boundaries, with the other two spatial directions simulated with periodic boundary conditions (see Fig. 5). Here, STTs form strong, distinct layers of a diamond-type structure, which is not observed in the bulk on the time scale of our simulations. While a crystal related to diamond is the most densely packed structure for STTs at high pressures,[33] it is all but inaccessible at moderate pressures,[53] where the assembly becomes frustrated prior to reaching the densest-packed structure. Through these simulations, we see that the presence of walls encourages a structure that is markedly different from that seen in the bulk. The diamond-type crystals formed in contact with flat walls have their $\{111\}$ plane aligned with that wall, just as the $\{111\}$ plane aligns with the surface of spherical containers. Here, the presence of a zero-curvature wall allows the structure to coherently propagate throughout the container. Intriguingly, similar behavior has been observed experimentally in spherically confined cubic particles.[21] For these particles, as in the simulations here, a confining spherical wall causes the structure to separate into a bulk-like core and a surface layer curved such that a flat polyhedral facet stays aligned with the wall. Here, we extend that observation to propose that under certain conditions, this surface layer may actually be able to stimulate the formation of a new structure, distinct from the unconfined bulk.

By calculating the fraction of different particle neighborhoods across different system sizes and confinement geometries, as well as different particle shapes, these observations can be quantified. Figure 6 illustrates the fractions of particle neighborhoods that are of the anti-aligned type (see Fig. 6a) and aligned type (see Fig. 6b) for a range of truncations. Note that here truncations of $c < 1.4$ are excluded, as they assemble a different phase with local motifs that are distinct from those contrasted here.[54] For spherical confinement, the prevalence of anti-aligned motifs increases with container size for $c \leq 2.0$, and correspondingly the prevalence of aligned motifs decreases. The anti-aligned motif is most common in the flat-walled case for these shapes, with the quenched bulk showing a decreased prevalence. The change is most pronounced for STTs at $c = 2.0$, for which the bulk system is dominated by the aligned motif, but in the presence of a hard, flat wall is dominated by the anti-aligned motif. For all shapes that assemble a diamond-type structure, the flat wall increases the degree of crystalline order and therefore the prevalence of anti-aligned motifs. Correspondingly, aligned motif prevalence for these shapes is suppressed and reaches a minimum between flat walls. By contrast, the frequency of the aligned motif increases slightly with system size in large containers for $c > 2.0$, but does *not* peak in the flat-walled case; instead, these shapes behave nearly identically to the unconfined bulk and in very large spherical containers.

4 Discussion

The primary distinguishing feature of spherically-confined hard-particle systems of truncated tetrahedra is the number of layers of particles that fit between the center of the container and its outer boundary. The distinct organization into concentric shells drives the structure towards local motifs that conform to the container wall.

While Platonic tetrahedra do not exhibit a transition between small-N and bulk behavior, owing to the fact that the same local motif dominates both types of systems, the other investigated shapes exhibit a gradual transition between different structural behaviors as the curvature of the container changes. At small numbers of particles—and therefore small containers with large curvatures—the aligned motif is favored, while at large particle numbers—with larger containers and smaller curvatures—the developing shell structures increasingly exhibit anti-aligned local motifs in highly-truncated particles.

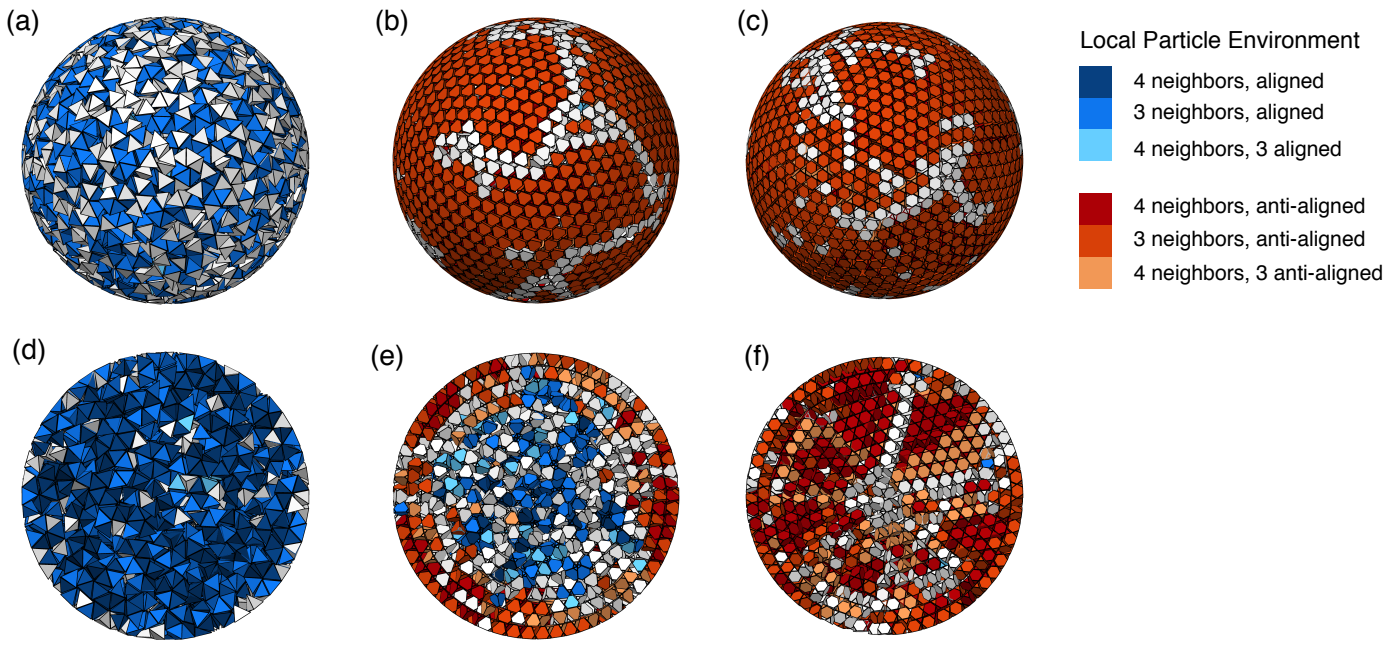

Fig. 4 Simulations of $N = 10,000$ particles with PT, STT, and ATT shapes in spherical containers, **(a–c)** viewed from the outside, and **(d–f)** as cross sections (**(a,d)** PTs, **(b,e)** STTs, and **(c,f)** ATTs). Coloration corresponds to the local particle environments: shades of blue represent predominantly aligned environments (70.5°) and shades of orange correspond to predominantly anti-aligned environments (90°). Deeper colors indicate that an increasing number of (up to 4) neighbors have the same misorientation angle as the central particle. White particles exhibit ambiguous, uncategorized environments. PTs have mostly aligned environments, with only the outermost shell influenced by the container. For ATTs and STTs, the outermost shells **(b,c)** are predominantly anti-aligned. The diamond-like structure expected from the anti-aligned motif is curved to fill the surface. For ATTs, this motif continues towards the interior **(f)**, but for STTs the layering breaks down, and near the center of the container the aligned motif dominates **(e)**.

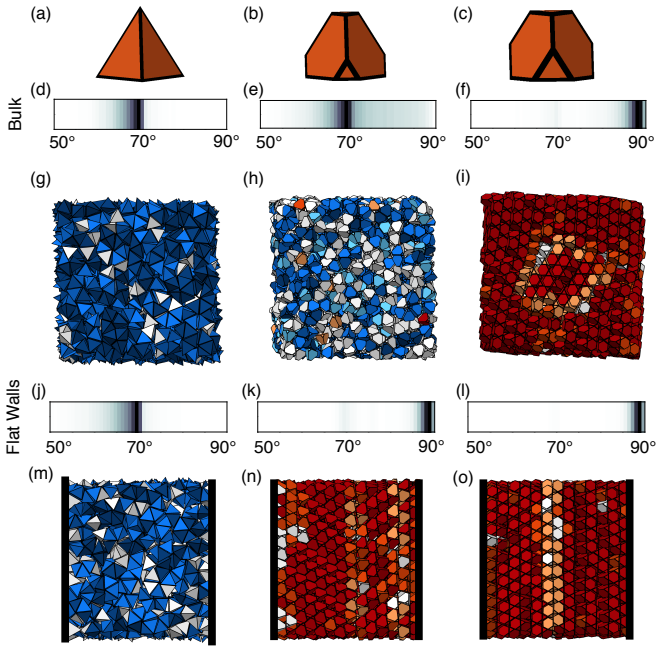

Fig. 5 The effect of flat confining walls on particle environment as compared to the bulk. Heatmaps show the distribution of misorientation angles for **(a–c)** PTs, STTs, and ATTs in bulk **(d–f)** and with flat walls in one dimension **(j–l)**. Note that flat walls have a small effect on motifs on PTs and ATTs, whereas for STTs the bulk system is dominated by the aligned motif **(e)** but for the flat walls the anti-aligned motif is prevalent **(f)**. Simulation snapshots show representative samples from bulk simulations **(f–i)** and confined ones **(m–o)**, with the walls highlighted in black. The change between aligned environments and anti-aligned ones can be seen in the STT systems **(h,n)**. Note that confined STTs and ATTs **(n,o)** exhibit $\{111\}$ layers aligned with the confining walls, whereas the crystal orientation in the bulk is random **(i)**.

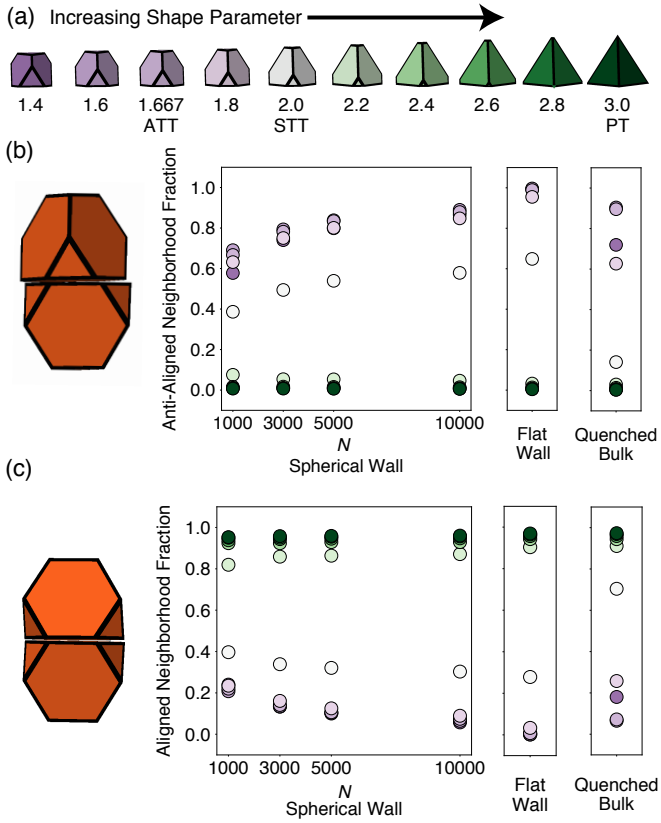

Fig. 6 The fraction of particle neighborhoods of **(a)** different particle shapes that are **(b)** anti-aligned and **(c)** aligned. Shown for comparison are spherically confined systems, systems confined between flat walls, and the bulk. Anti-aligned neighborhoods increase in prevalence for shape parameters $c \leq 2.0$ as system size increases, and the maximum fraction occurs in the flat-walled case. The quenched bulk assemblies tend to exhibit a lower prevalence of ordered motifs. STTs (displayed by white markers) undergo the most dramatic change, with confined systems exhibiting a predominantly anti-aligned environment, while the quenched bulk is predominantly aligned.

This phenomenon can be understood through the relationship between the curvature of the container and the particle arrangements. The aligned motif assembles into pentagonal bipyramids in which the large facet of each particle is at an angle to its neighbors (approximately 39° in the ideal motif for ATTs). The anti-aligned motif, conversely, has each large facet of the particles meeting its neighbor to form a flat plane; this forms the {111} plane in the diamond-type structure. We propose that the aligned motif is thus better suited to conforming to a curved surface, causing it to be favored near high-curvature walls. In small containers, clustered vertices fill the interior, maximizing packing density. On the other hand, in containers with a small curvature relative to the particle size, the flat plane of the anti-aligned motif can more easily pack along the surface. The motif imposed by the wall then seeds the growth of the assembled structure toward the center of the container.

Assembly in a container with flat walls promotes the growth of large, well-ordered crystals for ATTs (see Fig. 5). Additionally, for shapes such as STTs, which do not normally assemble ordered structures, we see that the presence of a flat wall induces the formation of a diamond-type crystal. This crystal spans the simulation box, significantly larger than any type of order we have observed in the bulk for this particle shape. Additionally, this method induces a reproducible texture in the crystal grain orientation. It is interesting to note that a previous study was similarly able to induce crystallization *via* "doping" the system with particles constrained in anti-aligned dimers that seed the corresponding structure locally.[53] Here, we show that there exists a different mechanism of affecting assembly with a global change, rather than a local one, and which provides an additional level of control over particle and grain orientations. This observation provides a potential pathway for structural selection in colloidal particles. By choosing an appropriate container, it appears to be possible to promote the growth of large, well-ordered crystals, even in systems of particles that do not typically assemble ordered structures. Conversely, if a disordered system is *preferred* for functional reasons, we suggest that container walls incompatible with the structure can frustrate crystallization, and can potentially propagate disorder throughout the system if the container size is chosen appropriately.

5 Conclusions

The properties of a material—in particular optical properties—can be very sensitive to the arrangement of particles with respect to their local environment, disorder, and filling fraction.[56–58] We show that the effect of container curvature on the local particle motifs in confined assemblies of hard tetrahedral shapes provides a mechanism for tuning the assembled structure relative to bulk materials.

The same particle can exhibit different local environments depending on the container in which it is confined during assembly, providing opportunities for controlling the assembled structure and function. In large systems, a container can "pattern" particle assemblies, causing the surface structure to be notably different from the interior, as well as from an unconfined bulk system. Interestingly, this observation that the system tends to order from the surface inwards is corroborated in some experimental studies of hard particles,[16,21,24] but reversed in others.[25] While this phenomenon is not explored in detail here, the potential difference in assembly pathways provokes a need for future study.

In this study the containers fluctuate, allowing them to adapt to the structure being assembled. In contrast, other studies fix the container size and study how the structure changes as the container size is varied—as opposed to varying the particle number.[26] In the fixed case, the structures observed depend on the mismatch between the periodicity of the target structure and the container, and can enforce new structures to fill that container. Here, we see a similar result—the assembly of structures not seen in an infinite system—but with slightly different boundary conditions and system parameters.

Our findings have implications for assembly mechanisms for core–shell-type particles, which have different properties on the surface and in the interior. In addition, precise control of colloidal particle size and geometry is a difficult task; here we show that particles with a shape that does not typically self-assemble into ordered crystals can be induced to do so through contact with an appropriate confining wall, potentially providing a route for the directed assembly of crystals from non-ideal constituents.

Future work will explore confinement geometries beyond those investigated in this study, as well as the interactions of this geometry with a wider selection of particle shapes. We have shown that the influence of the container holding a dense assembly cannot be discounted. It is critical to study the influence of container curvature on the wide array of common particle shapes that feature varying interparticle facet arrangements and local environments to make the most use of our toolkit in directed structure assembly.

Citation Diversity Statement

Recent work in several fields of science has identified a bias in citation practices such that papers from women and other minority scholars are under-cited relative to the number of such papers in the field (*e.g.*,[59–61]). In order to begin to provide transparency and accountability for citation gender imbalance,[62] we used an open-source code that predicts the gender of the first and last author of each reference by using databases that store the probability of a first name being carried by a woman.[60,63] Much to our regret, this method cannot account for intersex, non-binary, or transgender people. Excluding self-citations, our references contain 9.43% woman(first)/woman(last), 27.85% man/woman, 5.66% woman/man, and 57.05% man/man by this measure. (This method is limited in that names, pronouns, and social media profiles used to construct the databases may not, in every case, be indicative of gender identity.)

Author Contributions

R. S. S. and J. D. designed and performed the research. R. S. S., E. G. T., and J. D. conducted the analyses. R. S. S., E. G. T., and J. D. wrote the manuscript.

Conflicts of interest

There are no conflicts to declare.

Acknowledgements

R. S. S. acknowledges support from the National Science Foundation Graduate Research Fellowship under Grant No. DGE 2139899 (2021–2022) and DGE 1650441 (2020–2021). The authors would like to thank Professor Richard D. Robinson and Naomi R. Nelson for helpful discussions, and Professor Chrisy Xiyu Du for assistance with defining the particle geometry. This work was performed in part at the Cornell NanoScale Facility, a member of the National Nanotechnology Coordinated Infrastructure (NNCI), which is supported by the National Science Foundation (Grant No. ECCS-2025233). This work used the Extreme Science and Engineering Discovery Environment (XSEDE)[64], which is supported by National Science Foundation grant number ACI-1548562; XSEDE award DMR 190048.

Notes and references

1 J. Kepler, *De Nive Sexangula*, Godefridum Tambach, 1611.
2 T. C. Hales, *Annals of Mathematics*, 2005, **162**, 1065–1185.
3 P. Bartlett, R. H. Ottewill and P. N. Pusey, *Phys. Rev. Lett.*, 1992, **68**, 3801–3804.
4 J. K. Kummerfeld, T. S. Hudson and P. Harrowell, *The Journal of Physical Chemistry B*, 2008, **112**, 10773–10776.
5 P. F. Damasceno, M. Engel and S. C. Glotzer, *Science*, 2012, **337**, 453–457.
6 E. R. Chen, D. Klotsa, M. Engel, P. F. Damasceno and S. C. Glotzer, *Phys. Rev. X*, 2014, **4**, 011024.
7 D. Chen, Y. Jiao and S. Torquato, *The Journal of Physical Chemistry B*, 2014, **118**, 7981–7992.
8 Y.-J. Kim, J.-H. Kim, I.-S. Jo, D. J. Pine, S. Sacanna and G.-R. Yi, *Journal of the American Chemical Society*, 2021, **143**, 13175–13183.
9 M. Schweiger, T. Yamamoto, P. J. Stang, D. Bläser and R. Boese, *The Journal of Organic Chemistry*, 2005, **70**, 4861–4864.
10 C.-Y. Chiu, C.-K. Chen, C.-W. Chang, U.-S. Jeng, C.-S. Tan, C.-W. Yang, L.-J. Chen, T.-J. Yen and M. H. Huang, *Journal of the American Chemical Society*, 2015, **137**, 2265–2275.
11 M. A. Boles and D. V. Talapin, *Journal of the American Chemical Society*, 2014, **136**, 5868–5871.
12 I. Kacem, M. Hifi and R. M'Hallah, *Advances in Operations Research*, 2009, **2009**, 150624.
13 R. M'Hallah, A. Alkandari and N. Mladenovic, *Computers & Operations Research*, 2013, **40**, 603–615.
14 J. Wang, C. F. Mbah, T. Przybilla, B. Apeleo Zubiri, E. Spiecker, M. Engel and N. Vogel, *Nature Communications*, 2018, **9**, 5259.
15 V. N. Manoharan, M. T. Elsesser and D. J. Pine, *Science*, 2003, **301**, 483–487.
16 G. Zhu, L. Gao, Z. Xu, X. Dai, X. Zhang and L.-T. Yan, *Nano Letters*, 2021, **21**, 8439–8446.
17 C. Wensrich, *Powder Technology*, 2012, **219**, 118–127.
18 A. Mughal, H. K. Chan, D. Weaire and S. Hutzler, *Phys. Rev. E*, 2012, **85**, 051305.
19 E. G. Teich, G. van Anders, D. Klotsa, J. Dshemuchadse and S. C. Glotzer, *Proceedings of the National Academy of Sciences*, 2016, **113**, E669–E678.
20 V. Thapar, T. Hanrath and F. A. Escobedo, *Soft Matter*, 2015, **11**, 1481–1491.
21 D. Wang, M. Hermes, R. Kotni, Y. Wu, N. Tasios, Y. Liu, B. de Nijs, E. B. van der Wee, C. B. Murray, M. Dijkstra and A. van Blaaderen, *Nature Communications*, 2018, **9**, 2228.
22 O. D. Velev, K. Furusawa and K. Nagayama, *Langmuir*, 1996, **12**, 2374–2384.
23 E. Lauga and M. P. Brenner, *Phys. Rev. Lett.*, 2004, **93**, 238301.
24 B. de Nijs, S. Dussi, F. Smallenburg, J. D. Meeldijk, D. J. Groenendijk, L. Filion, A. Imhof, A. van Blaaderen and M. Dijkstra, *Nature Materials*, 2015, **14**, 56–60.
25 D. Wang, T. Dasgupta, E. B. van der Wee, D. Zanaga, T. Altantzis, Y. Wu, G. M. Coli, C. B. Murray, S. Bals, M. Dijkstra and A. van Blaaderen, *Nature Physics*, 2021, **17**, 128–134.
26 M. R. Khadilkar and F. A. Escobedo, *Soft Matter*, 2016, **12**, 1506–1516.
27 J. Mittal, J. R. Errington and T. M. Truskett, *The Journal of Physical Chemistry B*, 2007, **111**, 10054–10063.
28 J. Mittal, J. R. Errington and T. M. Truskett, *The Journal of Chemical Physics*, 2007, **126**, 244708.
29 A. Jaoshvili, A. Esakia, M. Porrati and P. M. Chaikin, *Phys. Rev. Lett.*, 2010, **104**, 185501.
30 I. B. Liu, N. Sharifi-Mood and K. J. Stebe, *Philosophical Transactions of the Royal Society A: Mathematical, Physical and Engineering Sciences*, 2016, **374**, 20150133.
31 M. Huang, C.-H. Hsu, J. Wang, S. Mei, X. Dong, Y. Li, M. Li, H. Liu, W. Zhang, T. Aida, W.-B. Zhang, K. Yue and S. Z. D. Cheng, *Science*, 2015, **348**, 424–428.
32 A. Haji-Akbari, M. Engel, A. S. Keys, X. Zheng, R. G. Petschek, P. Palffy-Muhoray and S. C. Glotzer, *Nature*, 2009, **462**, 773–777.
33 P. F. Damasceno, M. Engel and S. C. Glotzer, *ACS Nano*, 2012, **6**, 609–614.
34 K. M. Ho, C. T. Chan and C. M. Soukoulis, *Phys. Rev. Lett.*, 1990, **65**, 3152–3155.
35 *http://glotzerlab.engin.umich.edu/hoomd-blue/*, `http://glotzerlab.engin.umich.edu/hoomd-blue/`.
36 J. A. Anderson, C. D. Lorenz and A. Travesset, *J. Comput. Phys.*, 2008, **227**, 5342–5359.
37 J. A. Anderson, M. E. Irrgang and S. C. Glotzer, *Computer Physics Communications*, 2016, **204**, 21–30.
38 J. A. Anderson, J. Glaser and S. C. Glotzer, *Computational Materials Science*, 2020, **173**, 109363.
39 C. S. Adorf, P. M. Dodd, V. Ramasubramani and S. C. Glotzer, *Computational Materials Science*, 2018, **146**, 220–229.
40 Vyas Ramasubramani, Carl S. Adorf, Paul M. Dodd, Bradley D. Dice and Sharon C. Glotzer, Proceedings of the 17th Python in Science Conference, 2018, pp. 152 – 159.
41 C. S. Adorf, V. Ramasubramani, B. D. Dice, M. M. Henry, P. M. Dodd and S. C. Glotzer, *glotzerlab/signac*, 2019, `https://doi.org/10.5281/zenodo.2581327`.
42 *https://freud.readthedocs.io/*.

43 V. Ramasubramani, B. D. Dice, E. S. Harper, M. P. Spellings, J. A. Anderson and S. C. Glotzer, *Computer Physics Communications*, 2020, **254**, 107275.

44 A. Stukowski, *Modelling and Simulation in Materials Science and Engineering*, 2010, **18**, 015012.

45 A. Stukowski, *OVITO*, https://www.ovito.org.

46 *https://github.com/glotzerlab/plato.git/*.

47 G. van Anders, D. Klotsa, N. K. Ahmed, M. Engel and S. C. Glotzer, *Proceedings of the National Academy of Sciences*, 2014, **111**, E4812–E4821.

48 G. van Anders, N. K. Ahmed, R. Smith, M. Engel and S. C. Glotzer, *ACS Nano*, 2014, **8**, 931–940.

49 E. S. Harper, G. van Anders and S. C. Glotzer, *Proceedings of the National Academy of Sciences*, 2019, **116**, 16703–16710.

50 P. Meakin, H. Metiu, R. G. Petschek and D. J. Scalapino, *The Journal of Chemical Physics*, 1983, **79**, 1948–1954.

51 D. Frenkel and B. Smit, *Understanding molecular simulation: from algorithms to applications*, Academic Press, 2002.

52 A. S. Karas, J. Dshemuchadse, G. van Anders and S. C. Glotzer, *Soft Matter*, 2019, **15**, 5380–5389.

53 E. G. Teich, G. van Anders and S. C. Glotzer, *Nature Communications*, 2019, **10**, 64.

54 D. Klotsa, E. R. Chen, M. Engel and S. C. Glotzer, *Soft Matter*, 2018, **14**, 8692–8697.

55 W. Steurer and J. Dshemuchadse, in *Intermetallics – Structures, Properties, and Statistics*, Oxford University Press, 2016, ch. 7.4.3 Laves phases and related polytypes, pp. 252–258.

56 C. Noguez, *The Journal of Physical Chemistry C*, 2007, **111**, 3806–3819.

57 B. Gao, G. Arya and A. R. Tao, *Nature Nanotechnology*, 2012, **7**, 433–437.

58 S. Y. Lee, L. Hung, G. S. Lang, J. E. Cornett, I. D. Mayergoyz and O. Rabin, *ACS Nano*, 2010, **4**, 5763–5772.

59 N. Caplar, S. Tacchella and S. Birrer, *Nature Astronomy*, 2017, **1**, 0141.

60 J. D. Dworkin, K. A. Linn, E. G. Teich, P. Zurn, R. T. Shinohara and D. S. Bassett, *Nature Neuroscience*, 2020, **23**, 918–926.

61 P. Chatterjee and R. M. Werner, *JAMA Netw Open*, 2021, **4**, e2114509.

62 J. Dworkin, P. Zurn and D. S. Bassett, *Neuron*, 2020, **106**, 890–894.

63 D. Zhou, E. J. Cornblath, J. Stiso, E. G. Teich, J. D. Dworkin, A. S. Blevins and D. S. Bassett, *Gender Diversity Statement and Code Notebook v1.0*, 2020, `https://zenodo.org/record/3672110#.XrcgaS-z2nc`.

64 J. Towns, T. Cockerill, M. Dahan, I. Foster, K. Gaither, A. Grimshaw, V. Hazlewood, S. Lathrop, D. Lifka, G. D. Peterson, R. Roskies, J. R. Scott and N. Wilkins-Diehr, *Computing in Science & Engineering*, 2014, **16**, 63–74.